Chitosan-Tricarbocyanine Based Nanogels Were Able to Cross the Blood Brain Barrier Showing Its Potential as a Targeted Site Delivery Agent

Emilio Rivera López , Cecilia Samaniego López , Carla C. Spagnuolo , Bruno G. Berardino , Agustina Alaimo , Oscar E Pérez *

Posted Date: 6 June 2024

doi: 10.20944/preprints202406.0338.v1

Keywords: chitosan; tricarbocyanines; nanogels; SH-SY5Y cell line; blood-brain-barrier

 doi:10.20944/preprints202406.0338.v1

Article

Chitosan-Tricarbocyanine Based Nanogels Were Able to Cross the Blood Brain Barrier Showing Its Potential as a Targeted Site Delivery Agent

Emilio Rivera López [1], Cecilia Samaniego López [2,3], Carla C. Spagnuolo [2,4], Bruno G. Berardino [1,3], Agustina Alaimo [1,3] and Oscar E. Pérez [1,3,*]

[1] Departamento de Química Biológica, Facultad de Ciencias Exactas y Naturales, Universidad de Buenos Aires, Argentina; eriveralopez@qb.fcen.uba.ar (E.R.L.); bberardino@qb.fcen.uba.ar (B.G.B.); aalaimo@qb.fcen.uba.ar (A.A.)
[2] Departamento de Química Orgánica, Facultad de Ciencias Exactas y Naturales, Universidad de Buenos Aires, Argentina; cecisamaniego@qo.fcen.uba.ar (C.S.L.); carlacs@qo.fcen.uba.ar (C.C.S.)
[3] IQUIBICEN-CONICET
[4] CIHIDECAR-CONICET
* Correspondence: oscarperez@qb.fcen.uba.ar; Tel.: (+54-11) 4788-5755 / 528-58710

Abstract: Targeting drugs to the central nervous system (CNS) is challenging due to the presence of the blood-brain barrier. (BBB). The cutting edge in nanotechnology generates optimism to overcome the growing challenges in biomedical sciences through effective engineering of nanogels. The primary objective of the present report was to develop and characterize biocompatible natural chitosan (CS)-based NG that can be tracked thanks to the tricarbocyanine (CNN) fluorescent probe addition of the biopolymer backbone. FTIR shed light on the chemical groups involved in the CS and CNN interactions and between CNN-CS with tripolyphosphate, the cross-linking agent. Both in vitro and in vivo experiments were carried out to determine if CS-NG can be utilized as therapeutic delivery vehicles directed towards the brain. An ionic gelation method was chosen to generate cationic CNN-CS-NG. DLS and TEM confirmed that these entities size fell into nanoscale. CNN-CS-NG was found to be non-cytotoxic as determined in the SH-SY5Y neuroblastoma cell line through biocompatibility assays. After cellular internalization, the occurrence of an endo-lysosomal escape (a crucial event for an efficient drug delivery) of CNN-CS-NG was detected. Furthermore, CNN-CS-NG administered intraperitoneally to female CF-1 mice were detected in different brain regions after 2 h of administration using fluorescence microscopy. To conclude, the obtained findings in the present report can be useful in the field of neuro-nanomedicine when designing drug vehicles with the purpose of delivering drugs to the CNS.

Keywords: chitosan; tricarbocyanines; nanogels; SH-SY5Y cell line; blood-brain-barrier

1. Introduction

Neurological disorders are the main cause of poor health and disability with a high prevalence in the world population [1,2]. Despite their worrying incidence, many of those disorders still do not have adequate pharmacological treatment, and both existing alternatives and those under development present certain limitations [2].

Drug delivery refers to the formulations, technologies, and systems to transport therapeutics as needed to achieve the desired effects safely and efficiently. Conventional drug delivery systems are usually accompanied by systemic side effects that are mostly attributed to their nonspecific biodistribution and uncontrollable drug release properties [3]. Furthermore, many of the drugs have low bioavailability and cell permeability because of their low water solubility. On the other hand, the

 doi:10.20944/preprints202406.0338.v1

central nervous system (CNS) is a specially protected region and the passage of substances through it is highly regulated by the blood-brain barrier (BBB) [4]. Although the BBB is a natural protection system, it is an obstacle to overcome when establishing a pharmacological treatment since drugs must be administered in high doses to reach acceptable concentrations in the brain. Ergo, the latter fact results in many drugs generating unwanted effects in peripheral organs [5]. On the other hand, it is important that drugs can exert their effects in specific subcellular regions to minimize side effects and maximize their pharmacological activity. Overall, there are limitations in neuropharmacology that highlight the need to generate new therapeutic alternatives.

Biomaterials-based engineered nanogels (NG) that have the potential to revolutionize the diagnosis and treatment of many diseases are optimal candidates to overcome these limitations by designing new strategies [6,7]. On the other hand, hydrogels (at nanometric scale: nanogels, NG), comprise a 3D cross-linked network of polymers chains. This type of nanostructures allows to increase the bioavailability of drugs in difficult-to-access target sites, e.g. BBB [6,8]. Today, there is a wide range of NGs proposed for its application in the neuroscience field with the ability to cross the BBB transporting molecules for therapeutic purposes [9,10].

Chitosan (CS) is a polycationic amino polysaccharide that has gained a great reputation as a new functional biomaterial due to its biocompatibility, non-toxicity, and outstanding biological properties. Furthermore, its high mucoadhesion distinguishes it, which is an essential property for controlled specific site drug release [11]. CS-based NG with attractive physical and biological features are promising effective vehicles for drug delivery, cell culture, bioimaging and therapy [12,13]. Nowadays, CS-based NG generated by ionic gelation method with tripolyphosphate (TPP) as a cross-linker, is a frequently implemented technique since its easy formulation, less toxicity with possibility for scaling up [14].

NG are too small to be directly detected by light microscopy. Thus, the main strategy employed to overcome this subject was to design fluorescent bright NG with detectable signal [15]. Fluorescent NG offer unique possibilities when excited a specific added chemical group on the biopolymer backbone emiting light in different spectral regions. NG can be designed combining brightness, biocompatibility, and selectivity with respect to specific tissues. Therefore, they can provide visualization of pathophysiology at scales ranging from subcellular to whole-organ levels. Due to their versatility, fluorescent NG are attractive platforms to implement in bioimaging in biology and medicine [16].

Based on the considerations above detailed, CS was firstly labelled with a tricarbocyanine (CNN), a fluorescent probe synthesized at a laboratory scale. Secondly, CNN-CS-NG were designed and characterized by the pertinent analytical techniques. Thus, the present report aims was to determine the potentiality CNN-CS-NG, proposed as drug or bioactive compound carriers, to reach and cross through BBB. To offer a complete approach concerning the NG applications, its biocompatibility and biodistribution were studied using *in vitro* and *in vivo* models.

2. Materials and Methods

2.1. Reagents

CS (192 kDa) was purchased in Parafarm® (Saporiti S.A.C.I.F.I.A., Buenos Aires, Argentina; Ref. # 11017A). Foetal bovine serum (FBS) and 3-(4,5-dimethyl-thiazol-2-yl)-2,5-diphenyl- tetrazolium bromide (MTT), 1-ethyl-3-(3-dimethylaminopropyl) carbodiimide (EDC), deuterium chloride solution (DCl), N,N-Dimethylformamide (DMF), 6-aminohexanoic acid, sodium tripolyphosphate (TPP), 4',6-diamidino-2-fenilindol (DAPI) and Mowiol® 4-88 Mw ~31000 were purchased from Sigma-Aldrich Co. (St. Louis, MO, USA). Dulbecco's Modified Eagle's Medium (DMEM), Trypsin-EDTA 0.5% (10X), Antibiotic-Antimycotic (penicillin, streptomycin, and Amphotericin B; 100X), GlutaMaxTM-l (L-alanine-L-glutamine; 100X), Non-Essential Amino Acids (Glycine, L-alanine, L-asparagine, L-aspartic acid, L-glutamic acid, L-proline, L-serine; 100X) were from Gibco (Carlsbad, CA, USA). Other reagents were of analytical grade. Ultrapure quality water was always used.

 doi:10.20944/preprints202406.0338.v1

1.2. Determination of Deacetylation Degree (DD, %) of CS

^{1}H-Nuclear Magnetic Resonance (NMR) spectra were recorded at room temperature (RT) in DCl 5% in D_2O as solvent using a Bruker AM-500 NMR instrument operating at 300 MHz for ^{1}H. The ^{1}H-NMR spectrum is referenced to the peak of the solvent D_2O at δ = 4.79 ppm. The percentage of DD was calculated by using the following equation:

$$DD\% = \left[1 - \frac{\frac{A\,(CH_3)}{3}}{\frac{A\,(H2-H6)}{6}}\right] x\ 100 \qquad Equation\ 1$$

where A(CH_3) is the area of the peak corresponding to the three protons of the acetyl group (δ = 1.835 ppm) and A(H2-H6) is the sum of integral intensities of protons H2-H6 of glucosamine and N-acetyl glucosamine units.

1.3. Synthesis of CNN Fluorescent Probe and CNN-Labelled CS

The fluorescent probe was synthesized in two steps. Chlorotricarbocyanine (Cl-CNN) was prepared according to the previously reported procedure [17]. Briefly, CNN COOH was synthesized from CNN Cl. Cl-CNN (0.1 g, 0.13 mmol) and 6-aminohexanoic acid (0.033 g, 0.26 mmol) were dissolved in DMF (5 mL) and the solution was heated at 80°C overnight, protected from light. The solvent was removed under vacuum yielding an intense blue residue which was purified by a chromatography column (Sephadex LH-20, MeOH). CS was covalently labelled with CNN COOH by the following procedure: a MeOH solution of CNN COOH (21.2 mg) and EDC (4.5 mg) was added dropwise to a 1% w/v solution of CS in aqueous acetic acid 1% v/v with stirring and allowed to react overnight. The reaction was dialysed against deionized water using a Spectra/por MW 12-14 KDa for 48 h until no free probe was detected by fluorescence spectroscopy [12,17] (Figure 1).

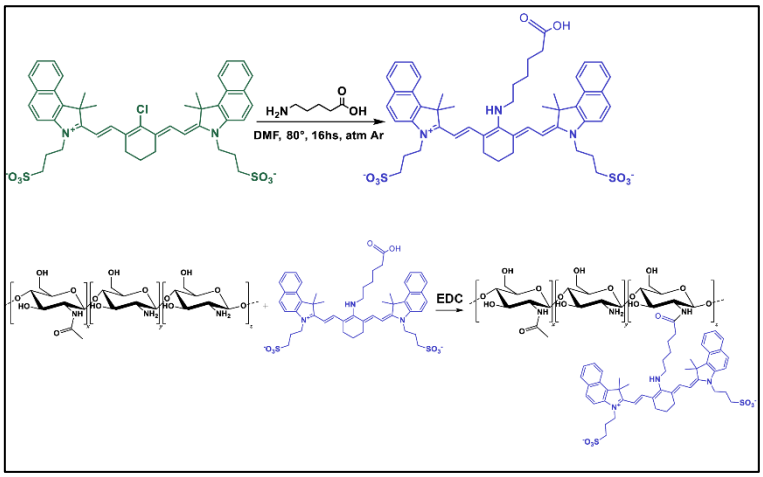

Figure 1. Schematic representation on the synthesis mechanism of CNN fluorescent probe (top) and diagram of the CNN labelling process to obtain CNN-CS biopolymer (bottom).

2.4. NG Generation

NG were prepared by ionic-gelation method [12,13]. Firstly, a stock solution of CS or CNN-CS (1% w/v) was dissolved in acetic acid solution (1% v/v). On the other hand, a TPP stock solution 2.5% w/w was prepared using ultra-pure water and filtered. Then, TPP was added dropwise under magnetic stirring to CS dissolution and a colloidal suspension was instantly obtained (Figure 2A). Then, non-labelled CS-based NG (CS-NG) which were used as control and CNN-CS-NG suspensions were subjected to high intensity ultrasound (HIUS) treatment for particles disaggregation under the conditions cited in Bihari et al., [18]. To this end, an ultrasonic processor (Polystat, Cole-Parmer, Vernon Hills, IL, USA) was used. Samples were HIUS treated with a maximum net power output of

 doi:10.20944/preprints202406.0338.v1

750 W at a frequency of 20 kHz with 20% of amplitude, during 5 min, a time stablished as adequate in previous contributions [13,19].

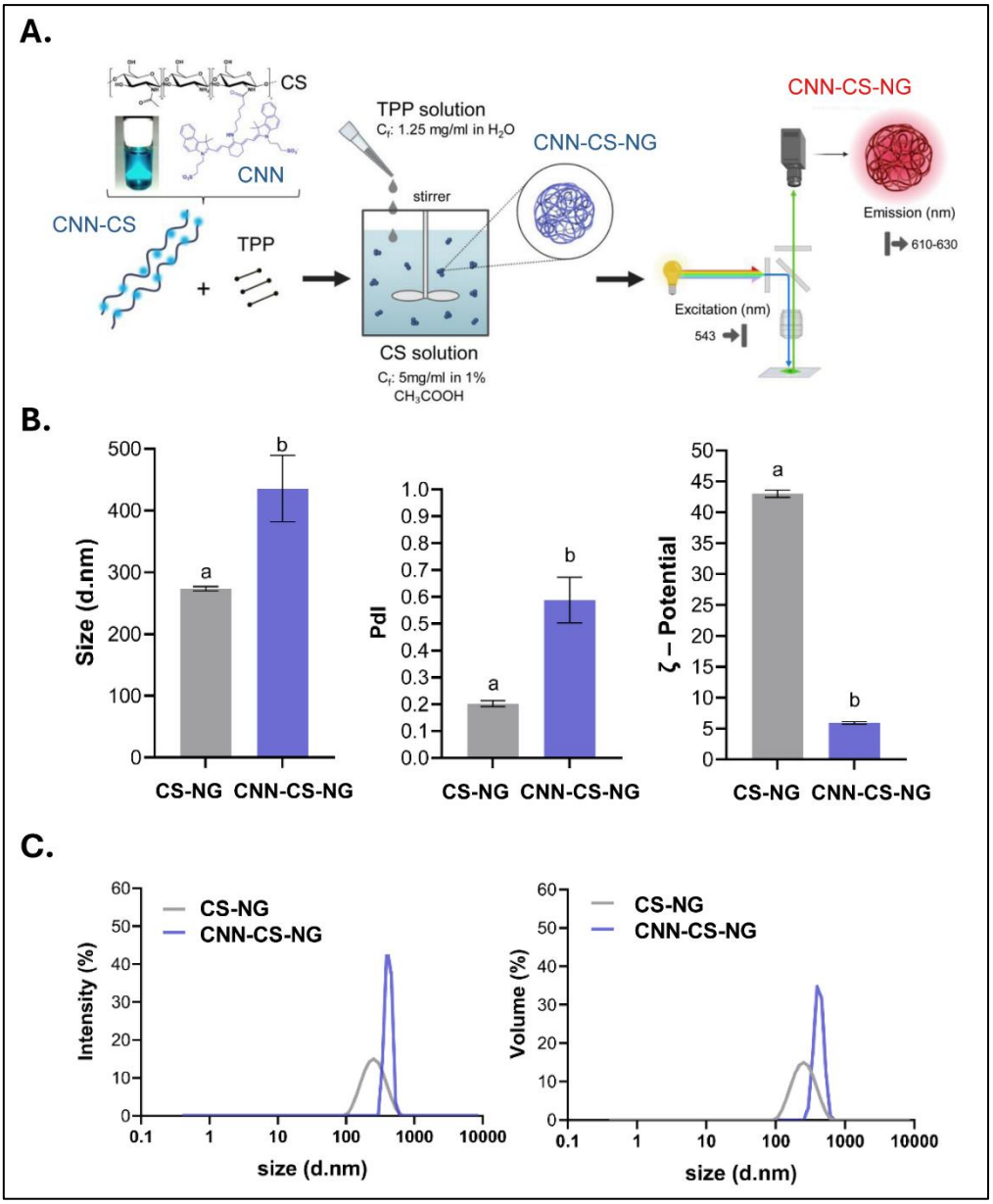

Figure 2. Formulation and physicochemical characterization of both CS-NG and CNN-CS-NG. **A.** Schematic drawing of the ionic gelation method for NG generation. After light excitation at λ= 543nm, CNN-CS-NG solutions emits at λ= 610-630nm **B.** Mean particle size, polydispersity index (PdI), and ζ-Potential for both CS-NG and CNN-CS-NG. **C.** Particle size distributions expressed in terms of intensity and volume. Different letters indicate significant differences between experimental groups ($p < 0.01$).

2.5. Characterizations of CCN-NG

2.5.1. Particle Size and ζ-Potential

Dynamic light scattering (DLS) with a scattering angle of θ=173° to the incident beam, Zetasizer Nano-ZSP, ZEN5600, Malvern Instruments (Worcestershire, UK) was employed. To obtain particle size distribution and polydispersityindex (PdI), samples were contained in disposable polystyrene cuvettes (DTS0012, Malvern Instruments, Worcestershire, UK). On the other hand, to determined ζ-potential values, samples were placed in disposable capillary cells (DTS1060, Malvern Instruments,

 doi:10.20944/preprints202406.0338.v1

Worcestershire, UK). The obtained data were analysed and interpreted accordingly to previous reports [12,13].

2.5.2. Fourier Transform Infrared Spectroscopy (FTIR)

Firstly, CS-NG and CNN-CS-NG samples were dried by lyophilization (The Virtis Company, INC, Gardiner NY, USA). Then, infrared spectra of each sample were recorded on an attenuated total reflectance FTIR-ATR Nicolet IS50 (Madison, WI, USA) (4000 – 400 cm−1; resolution 4 cm−1) from solids. Data was analysed based on the average of 32 scans and 4 cm-1 (PerkinElmer Spectrum 100; Thermo Scientific). The position and intensity of the absorption bands in the FTIR spectra were used to determine the functional groups in line with bibliography [20].

2.5.3. Transmission Electron Microscopy (TEM)

Particle morphology, distribution and shape were obtained directly by using a TEM Zeiss 109 with a Gatan W10000 camera (Carl Zeiss NTS GmbH, Oberkochen, Germany). Samples were applied onto a copper grid and air dried for 5 min at room temperature. Then, samples loaded grid was then negatively stained using 1% uranyl acetate for 90 s and air dried at room temperature and processed for microscopy analysis.

2.5.4. Confocal Laser Scanning Microscopy (CLSM)

For the visualization of CNN-CS-NG in solution, aliquots of 40 µL were placed in a 384 well glass-bottom black microplates. Fluorescence images were obtained on a Zeiss confocal LSM980 with Airyscan 2 using a 63×/1.4 objective (Zeiss, Oberkochen, Germany). The blue edition of the ZEN software was used for the processing and analysis of the images obtained. The sample was excited with a λ_{ex}=543nm and the emission was measured at a λ_{em}=639nm.

2.6. In Vitro Studies

2.6.1. Cell Culture Conditions

Human SH-SY5Y neuroblastoma cell line (ATCC® CRL-2266™) is widely used in neuroscience research as a neuronal cell model [21]. Cells were grown in DMEM supplemented with 10% heat-inactivated FBS, 2.0 mM glutamine, 1% non-essential amino acids, 1% penicillin/streptomycin/amphotericin B. Cells were maintained in a humidified atmosphere of 5% CO_2 - 95% air and 37°C. Medium was renewed three times *per* week. For experiments, cells were detached with trypsin-EDTA, diluted with DMEM 10% FBS and re-plated into multi-well plates to yield 70-80% confluent cultures after 24 h [22].

2.6.2. Cytotoxicity Assay

Growth cells in 96-well sterile culture plates were exposed to different concentrations of NG (10, 50, 100, 500µg/ml) for 24 h. Cell viability was evaluated by the metabolic MTT assay as previously described [13]. Absorbance was measured at λ=570 nm with background subtraction at λ=690 nm on a POLARstar Omega microplate reader (BMG LABTECH, Ortenberg, Germany).

2.6.3. Cellular Uptake

a) Fluorescence microscopy: cells were growth in Nunc™ 178599 Lab-Tek® Chamber Slide™ System, Glass, 16-Wells. CNN-CS-NG (50 µg/mL) were incubated in cells for 5, 15, 30, 60 min and 24h at culture conditions. After treatment, culture medium was removed, and cells were PBS-washed and fixed with 4% paraformaldehyde (PFA). After that, cells were incubated 10 min with DAPI for nuclei staining. [12]. Confocal images were acquired in a FV1000 Olympus confocal microscope (Olympus Inc., Japan). Same exposure times and camera settings were fixed for imaging under the same conditions. Disparities from different slides usually occur. For that reason, a non-specific signal, as an internal control for each sample, was considered: e.g., the

 doi:10.20944/preprints202406.0338.v1

average intensity of background signal outside of cells. Then, from the subtracted images, fluorescent mean intensity *per* cell can be measured by manually sketching out the cell boundaries. Also, the normalization of each cell's intensity was considered by multiplying the area factor. Data were rendered as the fluorescence intensity average determined by employing ImageJ software (NIH). In each experiment (n = 3), 25 cells were analysed from at least 4 randomly chosen fields for each treatment. Digital images were optimized for contrast and brightness using Adobe Photoshop 7.0 Software.

To quantify endo-lysosomal escape, fluorescence microscopy was used to provide information about intracellular fluorescence profiles (IFP). Cells were imaged, classified, and ranked by their NG uptake and endo-lysosomal escape efficiency was determined by using a previously described criterion [23,24]. A *punctate* fluorescence pattern is regularly considered as an indicator of the tracer compound being entrapped into vesicles, meanwhile a *moderate* and *diffuse* cytosolic staining implies leakage from the endo-lysosomes.

b) Flow cytometer: cells were growth in 12-well plates to be incubated then with CNN-CS-NG (50 µg/mL) for 5, 15, 30, 60 min and 24 h at culture conditions. After treatment, cells were washed with PBS, trypsinized, resuspended in PBS and immediately subjected to flow cytometry (FACS Aria Becton Dickinson). Mean fluorescence intensity of the cell population that internalized CNN-CS-NG was determined by using FlowJo v.10.7.2 software (TreeStar/BD Bioscience) [25].

2.7. In Vivo Studies

2.7.1. Animals

Female CF-1 mice (crlfcen:CF1) (ranging from 3 to 4 month of age and 30-52 g of body weight) obtained from the University of Buenos Aires Animal Facility (Bioterio Central, Facultad de Ciencias Exactas y Naturales, Argentina) were used for the *in vivo* experiments. Animals were housed in a room with controlled temperature (22 ± 1°C) and humidity (50% ± 10) under filtered positive-pressure ventilation. Animals were kept in a 12:12 h light:dark cycle with lights on at 6 am, and food and water were administered *ad libitum*. Experiments were performed in accordance with local regulations and the National Institutes of Health (NIH) Guide of the Care and Use of Laboratory Animals (NIH publication 80-23/96) and were previously approved by the Institutional Ethics Committee (CICUAL, Protocol No. 0024 - University of Buenos Aires) [26].

2.7.2. CNN-CS-NG Brain Uptake

Animals were randomly divided into three experimental groups, each group with N = 3, exposed according to the experimental setup [10,27]:

- Experimental groups: mice received an intraperitoneal (i.p.) injection with 200 µL solution containing 250 µg/mL or 1000 µg/mL of CNN-CS-NG.
- Control group: mice were injected i.p. with 200 µL of distilled water.

Mice were sacrificed 2 h after injection through cervical dislocation. Brains were immediately extracted from the skull, divided into hemispheres, and post-fixed by immersion in 4% PFA overnight at 4 °C. After that, hemispheres were transferred to PBS to cut them into 50 µm thick in a vibrating microtome (Pelco EasySlicer, Ted Pella Inc., Redding, Ca, USA). Sections were stored in a cryoprotectant solution (25% glycerol, 25% ethylene glycol, 50% PBS) at - 20°C until use. Sagittal sections were obtained yielding to consecutive slices and covering most of the brain [28,29]. All slices were stained with DAPI (1 µg/mL in PBS) for 10 min, mounted, and imaged on FV1000 Olympus confocal microscope (Olympus Inc., Japan).

To give a quantitative measurement, fluorescent images of brain sections were submitted to an image analysis software (ImageJ). Remarkably, for fluorescent quantification, images were not manipulated or over-exposed; that is to say, the potency of the laser, the excitation and emission ranges, the gain of signals, threshold limits and all other parameters were kept constant. For each

 doi:10.20944/preprints202406.0338.v1

treatment, the fluorescence intensity *x* area in 50 fields *per* sagittal slide was calculated. The folds increase in the mean fluorescence intensity was determined by subtracting the autofluorescence of the tissue as reference (control animals).

2.8. Statistical Analysis

Analyses were carried out by using GraphPad software (GraphPad Prism 8.4.3; GraphPad Software, Inc., La Jolla, CA). All data are presented as means ± Standard Error of Mean (SEM). Furthermore, one-way analysis of variance (ANOVA) test followed by Tukey post-hoc test to compare differences between multiple groups was applied. A value of $p<0.05$ was considered statistically significant.

3. Results

3.1. NG Characterization

The CS's DD is defined as the molar fraction of D-glucosamine in the polysaccharide chain composed of both N-acetylated glucosamine and D-glucosamine. DD is a key factor since it influences in the physicochemical features of the CS. There is general agreement in literature that ^{1}H NMR is the best and most accurate method currently available for DD determination [30]. CS with 55-70% of DD is considered a low-grade meanwhile 70-85% corresponds to a medium grade. CS with 85% - 95% is considered of high-grade and 95-99% of ultra-high grade. Particularly, CS with 100% of DD is difficult to produce [12]. Figure 1S showed the ^{1}H NMR spectrum that allowed to determine that the employed CS presented a DD equal to 95.4%. Therefore, the CS used in this report correspond to an ultra-high grade. The leitmotiv of the present report was to generate a NG that can cross the BBB. The proof of such a phenomenon will be the detection and observation of fluorescent NGin brain areas. Therefore, the physicochemical characteristics of CNN-CS-NG formulated were firstly examined.

Regarding to hydrodynamic diameter values, CS-NG, used as a control, and CNN-CS-NG exhibited a mean size centred in 273 ± 3.5 nm and 435 ± 53.8 nm, respectively. This significant increase represented around 1.55 times the average particle size because of the presence of the fluorescent probe. Polydispersity index (PdI) analysis revealed variations from 0.20 ± 0.01 (NG) to 0.58 ± 0.08 (CNN-CS-NG). Towards to ζ-Potential, NG presented a positive surface charge that decrease from 43.0 ± 1.2 in CS-NG to 5.9 ± 0.4 mV for CNN-CS-NG (Figure 2B). Results from DLS expressed the particle distribution size distribution in terms of intensity (%) and volume (%). Both graphs revealed a unique peak for the population analysed, that is, NG presented a monomodal distribution whose mean volume corresponded to the above informed (Figure 2C).

Figure 3 corresponds to TEM images revealed a spherical morphology with darker tone for both, CS-NG, and CNN-CS-NG cores. There was a higher tendency to form aggregates in the system constituted by CNN-NG, which could be explain the larger size of particles obtained with DLS. On the other hand, lower ζ-Potential implies lower electrostatic repulsion between particles with a manifest tendency to group in clusters [31].

 doi:10.20944/preprints202406.0338.v1

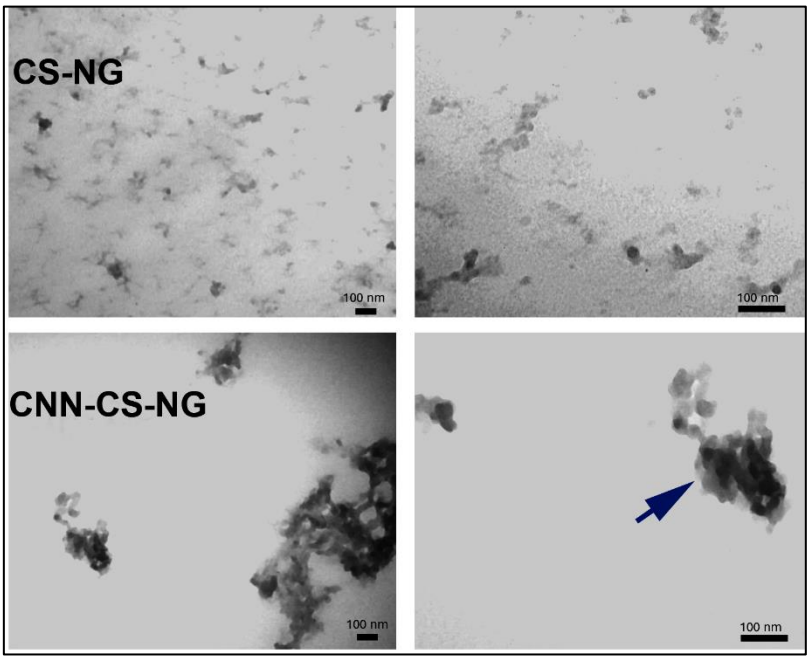

Figure 3. Ultrastructural characterization obtained by TEM of both CS-NG and CNN-CS-NG. Left: 50,000× magnification; Right: 85,000× Scale bar: 100 nm. Arrow indicate CS-NG and CNN-CS-NG aggregates.

Afterwards, the CNN-CS-NG were examined in aqueous solution using confocal microscopy. In agreement with the TEM technique, CNN-NG were observed forming aggregates that resembled the FITC-CS nanoparticles (NP) generated by Khattab et al., [31] (Figure 4).

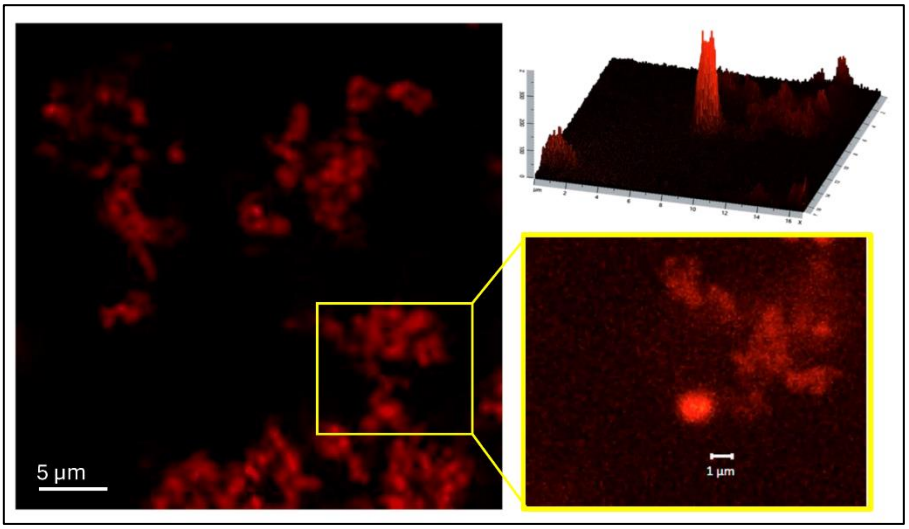

Figure 4. Confocal fluorescence microscopy images of CNN-CS-NG in aqueous solution (λ_{ex}= 543nm; λ_{em}= 620nm). Scale bar: 5 µm and 1 µm (zoom). Fluorescence profile plot (Zen Blue software).

Figure 5 correspond to the FTIR spectra obtained for free CS, NG, and CNN-NG. To organize the analysis, two comparisons were made: CS versus CS-NG and CS-NG versus CNN-CS-NG [32]. Progressing with the sample's characterization, FTIR spectra were obtained for free CS, NG, and CNN-CS-NG. To organize the analysis, two comparisons were made: CS versus CS-NG and CS-NG

 doi:10.20944/preprints202406.0338.v1

versus CNN-CS-NG. Thus, CS macromolecule shows its characteristic peaks at 3355 and 3288 cm^{-1}, typical of the O-H and N-H bonds stretching. At 2998 cm^{-1} correspond to characteristic peak at C-H stretching. At 1645 cm^{-1} there was a typical peak of the C=O stretching of the amide II group. At 1582 cm^{-1} was a specific peak of the vibration of an amine I (N-H bending of primary amine). At 1404 cm^{-1} was a characteristic peak of the C-H and O-H deformation in amide II. Later, at 1013 cm^{-1} appeared the corresponding peak of the C-O/C-H stretching [13]. In the NG spectrum, a peak at 3188 cm^{-1} was seen, a region where CS showed two peaks, indicating vibrational changes of the amino (N-H) and/or hydroxyl (O-H) group. Then, the peaks seen in the CS at 1645 and 1582 cm^{-1}, corresponding to the stretching of C-O (amide II) and N-H (amine I) bond, respectively, were shifted to 1635 and 1539 cm^{-1}. These changes have been described as proving the electrostatic interaction between CS and TPP molecules [33]. This functional group in principle would not be directly involved in the interaction. Finally, in the spectrum of the CS-NG, a peak is observed at 1219 cm^{-1}, which was not detected in the spectrum of the free CS macromolecule belongs to the presence of the P-O and/or P=O bond of the TPP's phosphate group [13]. Then, in the CNN-CS-NG sample, the peak of 3188 cm^{-1} presented in the CS-NG, shifts to 3265 cm^{-1}. This indicated vibrational changes in the amino (N-H) and/or hydroxyl (O-H) group. The peak at 1635 cm^{-1} in the CS-NG sample varies in those fluorescent NG (1625 cm^{-1}). Discrepancies could be explained by the covalent binding of CNN with the CS macromolecule since the union presumably formed between the biopolymer and the CNN converts the amine I of the deacetylated unit into an amide II group. Two peaks appeared in the CNN-CS-NG spectrum, one corresponding to the amide formed in the covalent bond between the CNN and CS, and another typical of the N-acetyl-glucosamine unit. So, the peak at 1539 cm^{-1} for the CS-NG, which corresponds to the amide group changes in CNN-CS-NG sample (1513 and 1549 cm^{-1}).

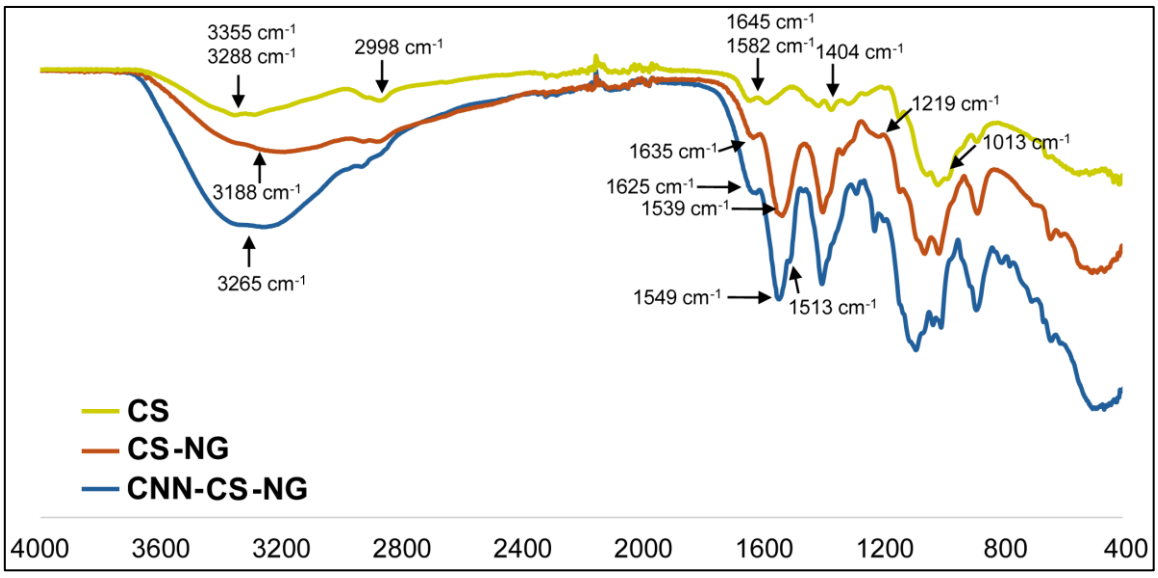

Figure 5. FTIR spectra for free CS molecule (yellow line), CS-NG (orange line) and CNN-CS-NG (blue line).

3.2. Biological Performance of CNN-CS-NG: Cellular Biocompatibility, Uptake, and Imaging

Next, the *in vitro* cytocompatibility of both CS-NG and CNN-CS-NG was investigated in the system formed by human SH-SY5Y neuronal cell line using the metabolic viability through MTT assay. As shown in Figure 6, no significant reduction in cell viability was found when the NG concentration was equal or less than 100 µg/mL up to 24 h of exposure. At the concentration of 500 µg/ml, cell viability was significantly reduced by 13.6% (CS-NG) and 22.2% (CNN-CS-NG). Also, cells suffered morphological changes since they lost cell-cell contact and rolled up rather than spreading out on the culture dish. Therefore, the obtained NG may not be considered harmful at a concentration less than 100 µg/mL for *in vitro* use.

 doi:10.20944/preprints202406.0338.v1

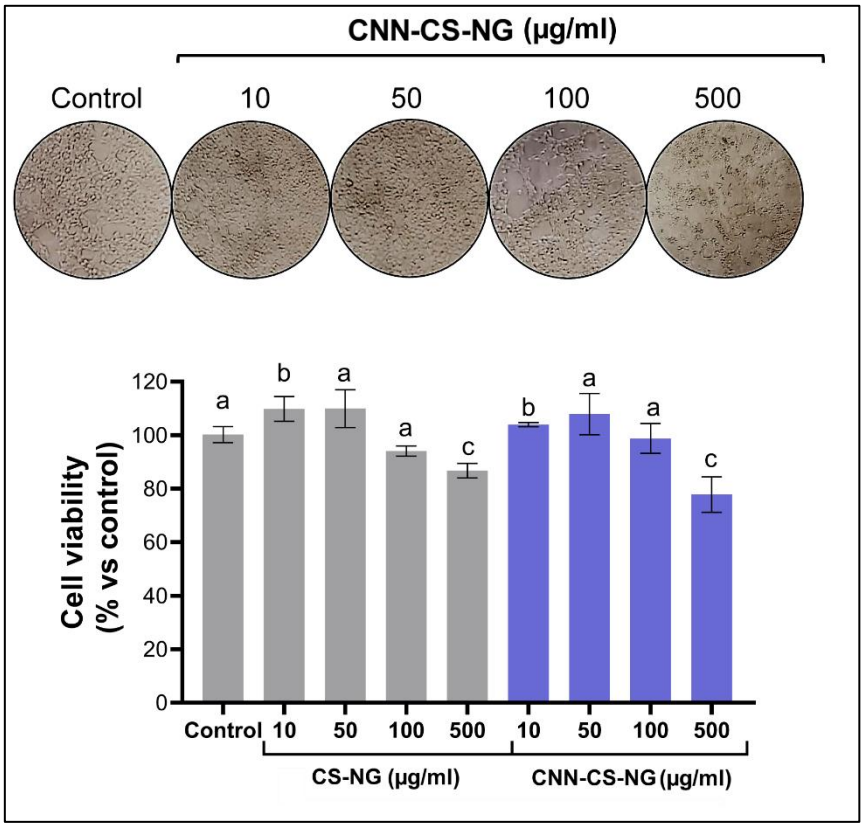

Figure 6. Phase-contrast microscopy images and MTT analysis corresponding to neuronal SH-SY5Y cell line. Different letters indicate significant differences between experimental groups ($p < 0.01$).

In nanomedicine, the safe entry of NP into cells would be a crucial step to obtain high therapeutic efficacy when they are used as drug carriers. Therefore, the understanding of the uptake and the intracellular trafficking of NG is crucial for their design and development. Particularly, it is imperative to design carriers with the abilities to escape of degradative vesicles. The latter phenomenon is called endo-lysosomal escape, and it has been well recognized as a major "bottleneck" in the drug delivery [24,34,35]. In the present report, the uptake capacity of the CNN-CS-NG (50 µg/ml) was studied as a function of time (0, 5, 15, 30, 60 min and 24 h). To this end, representative images at each time were observed and captured with epifluorescence microscopy. Figure 7A shows that cells incorporated the NG gradually over time and they are widely internalized after 24 h of incubation. Images were taken maintaining the same setting parameters (brightness, contrast, exposure time). Then, changes in fluorescence intensity were quantified as a measure of particle uptake. Maximum fluorescence intensity was achieved at the highest time considered (Figure 7B). NG internalizations were confirmed by flow cytometry which constitute a kinetic approach. After CNN-CS-NG treatment, the resulting histogram of the fluorescent probe channel shifted to higher intensities in a time-dependent manner, resulting in a significant increase in fluorescence intensity into the cells. Particularly, the quantification determined that the mean values of fluorescence intensity (A.U.) for each recorded time was 340 (5 min), 345 (15 min), 418 (30 min), 483 (60 min), and 2641 (24 h) (Figure 7C). Both, epifluorescence microscopy and cytometry techniques, corroborated that the CNN-CS-NG has successfully entered the cells as a function of time.

 doi:10.20944/preprints202406.0338.v1

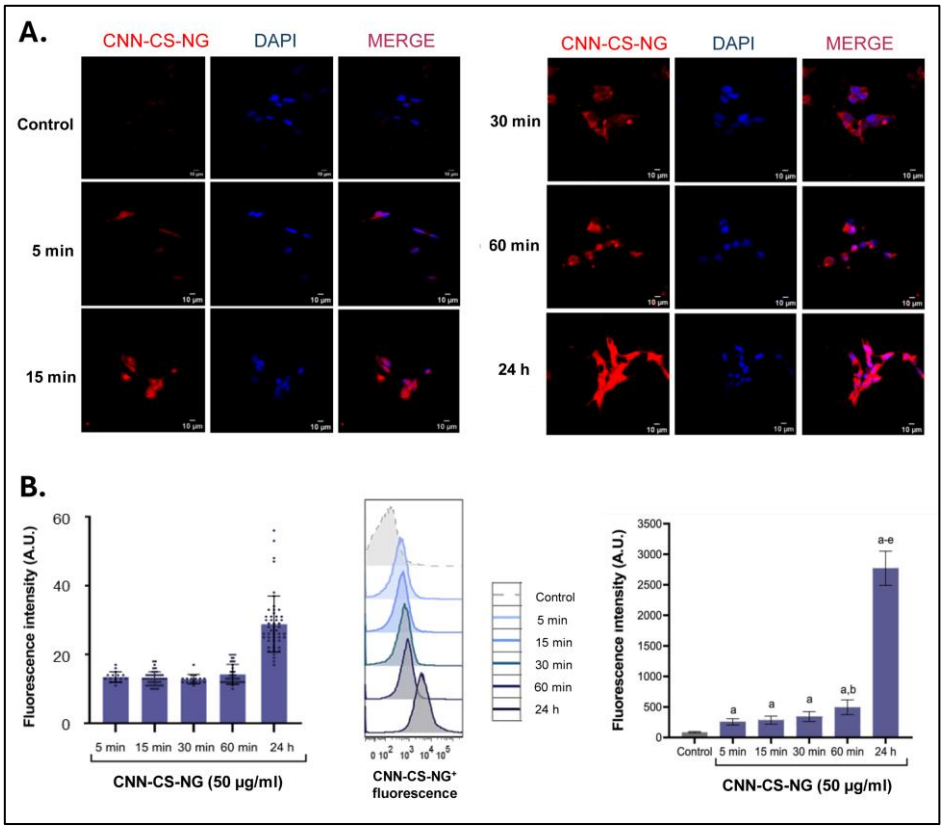

Figure 7. CLSM and flow cytometry analysis. **A.** The CLSM images of neuronal SH-SY5Y cell line incubated with 50 µg/ml CNN-CS-NG for different times at 37ºC. Each series can be sorted by the nuclei of cells being dyed in blue by DAPI, CNN NG and a merge of the two channels of both above, respectively. Scale bar: 10 µm. **B.** Mean fluorescence intensity bar-got plot. Dots represent the distribution of each quantify fluorescence intensity per cell determined from microscopy images. **C.** Left: representative flow cytometer histograms showing the population of CNN-CS-NG positive cells (blue scale) compared to the untreated control (gray). Right: quantification of the mean fluorescence intensity. Different letters indicate significant differences between experimental groups ($p < 0.01$).

Escape from endosomes/lysosomes was determined accordingly to ranking criteria previously described in section 2.6.3 (item a). A punctate fluorescence pattern is frequently considered a sign of the tracer compound being entrapped into the vesicles, while a diffuse cytosolic staining implies leakage from them [23,34]. Three IFP were detected and represented in Figure 8A: punctate, moderate, and high. Upon quantification, moderate and high IFP was mostly observed in cells after 24 h of CNN-CS-NP incubation in comparison to cells exposed for shorter time. Also, as the analysis time elapsed, it was feasible to detect the maturation of the endosomes and finally, the escape into the cytoplasm. This is the reason why it was concluded that at early incubation times, NG are endocytosed. Then, the cationic nature of the present nanosystem [12] would lead to the proton sponge effect resulting in extensive osmotic swelling and eventual physical rupture of the acidic vesicles (Figure 8).

 doi:10.20944/preprints202406.0338.v1

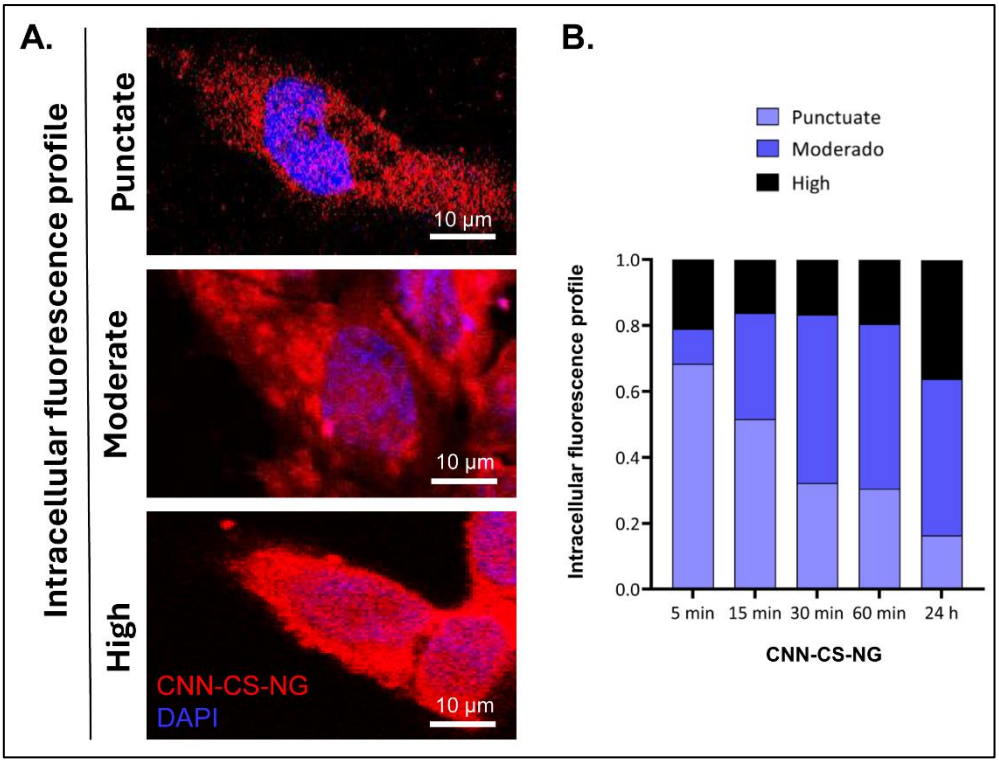

Figure 8. A. Intracellular fluorescence profile (IFP) illustrating the difference between a punctate pattern (sequestered carrier into vesicles) and moderate/diffuse staining (cytosolic carrier). Scale bar: 10 µm. **B.** Classification and counting of each pattern (N= 190 cells/experimental group).

Vermeulen et al., [36] observed that NG accumulate into the nucleus upon endo-lysosomal release. In line with these authors, we observed that SH-SY5Y cells exhibited red fluorescence into the cytosol and nucleus upon 24 h of incubation (Figure 9A and video S1). This observation was corroborated by drawing a line-scan profile of fluorescent intensity with ImageJ software (Figure 9B), which shows the red and blue signals coincident, suggesting the efficient nuclear uptake [37]. This can lead to the interpretation that CNN-CS-NG were spread all over the cytoplasm with a high amount in the nuclei.

 doi:10.20944/preprints202406.0338.v1

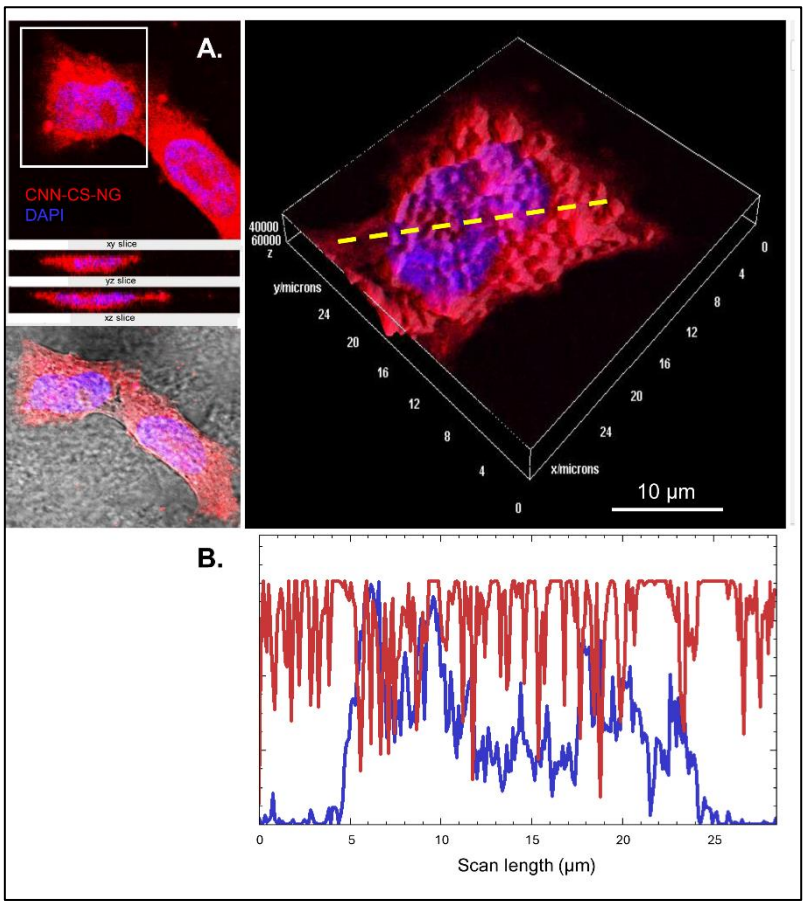

Figure 9. Intracellular localization of CNN-CS-NG in SH-SY5Y cells. **A.** CLSM images of cells incubated 24h with CNN-CS-NG (50 µg/ml) and stained by DAPI. **B.** Line-scan profile fluorescence intensity perform through yellow dotted line. Scale bar: 10 µm.

3.3. NG Reach the Mice Brains

The ability of the CNN-CS-NG to reach CNS tissues was evaluated in vivo in healthy mice. A diagram of the protocol followed can be seen in the Figure 10A. It was administered i.p. two concentrations of CNN-CS-NG (250 and 1000 µg/ml) and allowed to circulate for 2 h. The NG vehicle, distilled water, was used as a control (Figure 10A). Then, representative regions (cortex, striatum, hippocampus, and cerebellum) of the mouse brains were selected to examine whether CNN-CS-NG could be detected in sagittal slices (Figure 10B).

Figure 10C shows images taken with fluorescence microscopy of the above-mentioned brain sections after the administration of 1000 µg/ml compared to the corresponding control mouse brain. The results indicated that the mean fluorescence intensity was higher in brain regions that corresponds to those treated animals with 1000 µg/ml CNN-CS-NG. Meanwhile not obviously differences were observed between control and the 250 ug/ml CNN-CS-NG treated animals' group (Figure 2S). The results indicated a 3.2-fold increase in the cortex fluorescence, 2.5-fold in the cerebellum, and 2-fold in the striatal and hippocampal regions (Figure 10D). Remarkably, small perinuclear fluorescent spots were observed in samples after 2 h of administration (Figure 10E).

Preprints.org (www.preprints.org) | NOT PEER-REVIEWED | Posted: 6 June 2024 doi:10.20944/preprints202406.0338.v1

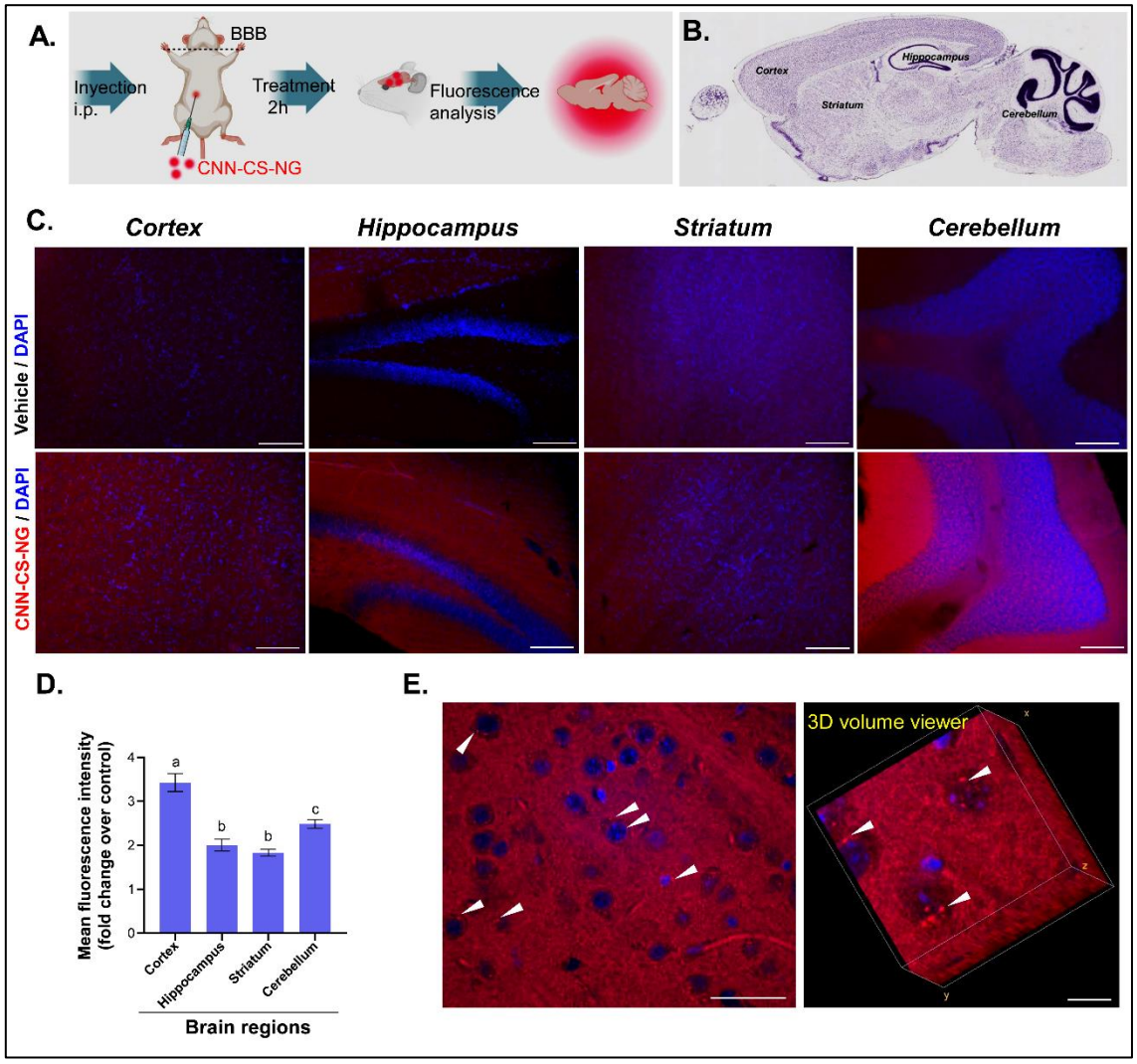

Figure 10. Images of different zones of mice brain. **A.** Simplified representation of the experimental protocol. **B** Nissl stained-sagittal section obtained from Allen Institute for Brain Science, Atlas Brain Map to show the brain regions analysed. **C.** Microscopic brain images of both control (vehicle) and 1000 μg/ml CNN-CS-NG-treated mice (magnification of 10X, Scale bar 100 μm). **D.** Quantification of the mean fluorescence intensities (Fold change of control. Bars show the mean ± SEM). Different letters indicate a statistically significant difference ($p < 0.01$). **E.** Left: confocal image showing CNN-CS-NG as red spots inside the nervous cells (probably neurons) indicated with arrowheads (magnification of 60X, scale bar: 50 μm); right: 3D volume viewer, scale bar: 10 μm.

4. Discussion

In the development of nanosystems for biomedical purposes, one of the most relevant issues, is the assessment of their capability to cross biological barriers (e.g. BBB), as well as their cellular uptake. Depending on the microscopy technique used (phase contrast microscopy, fluorescence microscopy, or TEM), NG can be made detectable by binding/loading appropriate dyes during the generation process or by labelling with specific histochemical stain after administration [38]. Developing tracking approaches for nanosystems with fluorescent probes is a main issue in nanomedicine and especially in targeted drug delivery systems [39]. Among them, CNN-based probes have optimal photophysical and photochemical properties due to their good biocompatibility and low toxicity in living systems, with a wide range of applications in biomedicine and biochemistry. Current studies revealed that the combination of the properties of CNN and NG lead to the generation of versatile model platforms that allowed the study of entrancing and metabolization of the nanosystem. Particularly, CNN-polymeric NG systems possesses potential as probes for several types of imaging

 doi:10.20944/preprints202406.0338.v1

techniques [17,40]. Therefore, in the present report, CNN-CS-NG have been designed by ionic gelation of CS-CNN biopolymer with the objective of identifying their potential to be use as drug carriers and delivery agents for neurological treatments.

Regarding the NG size range, the literature reports that nanocarriers that promoted drug deposition in brain tissue should vary between 50 and 200 nm [27]. It should be noted that these studies consider only dry and naked NG, with a size represented only by the core area, which do not really exist in biological fluids, where they exist with a hydration layer and modified by proteins that accumulate on their surfaces forming a crown that increases the hydrodynamic diameter of the particles. According to our results, the particle size that exceeded 200 nm was adequate in both the *in vitro* uptake and the *in vivo* BBB passage models. However, there are certain discrepancies in literature, e.g., Lombardo et al., mentioned in their review that NG size seems to have little impact in a size ranged, from 12 to 340 nm, into which the BBB crossing was possible [41]. Monge-Fuentes et al., obtained values of 340 nm for their albumin-PLGA NP and 470 nm when coupled with phthalocyanines [27]. In accordance with our system, the works cited confirmed that NG were able to reach the brain parenchyma, as was revealed by the fluorescence detection. Furthermore, and in agreement with our results, the increase in the hydrodynamic diameter observed in fluorescent NGs could be attributed to classical aggregation processes related to physicochemical factors previously described for phthalocyanines. Taking this hypothesis into consideration, we do not rule out that the increase in size of CNN-CS-NG could be due to the presence of CNN groups. In fact, CNN-CS-NG aggregates were observed using TEM and confocal microscopy. Nevertheless, the morphologies of these individual NG kept similar spherical structures. Analogous results were observed with FITC-CS NG and RBITC-CS NG generated by ionic gelation with TPP [42]. ζ-potential of CNN-CS-NG was slightly lower than those of the dye-free NG due to the consumption of amino groups by dye labelling, reaction that was confirmed by FTIR analysis. On the other hand, ζ-potential becomes a key parameter for the molecules that must cross cell membranes and particularly the BBB. This is due to the endothelial barrier and cytoplasmatic membrane of endothelial cell that has negative charges at physiological pH due to the presence of mucopolysaccharides, glycolipids, flucoproteins, proteoglycans, sialic acids, and sulphates [43]. In this sense, the electrostatic interaction between the positively charged part of the CNN-CS-NG and the negatively charges on the cell membrane could facilitate their absorption and transport through the endothelial cells, favouring their arrival to the brain parenchyma. Furthermore, Seko et al., reviewed that when ζ-potential is high enough, e.g., greater than ±30 mV, NGs repel each other. This event allows to reach a dispersed solution preventing agglomeration during NGs solution storage. Particularly, aggregation begins at ζ-potential values less than 5 mV [44]. At first, the tendency is to hypothesize that nanovehicles with ζ-potential value would not be able to cross the BBB. Nevertheless, fluorescent PEG-coated polystyrene NG with a ζ-potential less negative than -4 mV were able to diffuse consistently in fresh human brain cortex, fresh rat ex vivo and mouse brain in vivo [45]. Papadia et al. employing nanoliposomes with similar size (100-150 nm) but with different ζ-potential determined a significant difference in the uptake of liposomes with neutral and non-neutral surface charge in hCMEC/D3 brain endothelium. These authors found no substantial variation in the cellular uptake between liposomes with a ζ-potential variation between -2 and -16 mV. Also, the greatest nominees to overcome the BBB resulted the electrically neutral molecules [46]. In conclusion, it could be concluded that ζ-potential did not exert a guiding role in the internalization processes.

Biomaterials are considered raw materials of biological origin capable of treating, improving or supplanting tissues, organs, or functions in biological systems. These compounds play an increasingly important role in modern health application systems. Its biological impact is fundamental to the international standard ISO 10993-5, which provides guidelines for the choice of appropriate evaluations, such as: cell damage due to morphological changes, measurements of cell growth and/or specific aspects of cellular metabolism. All these techniques correspond to a classic approach that continue to be internationally accepted today [47]. Thus, cytotoxicity can be addressed from multiple responses at the cellular level, one of the most used being the tetrazolium salt assay, better known as MTT [47]. In this way, the effect of the tested concentrations of both CS-NG and

 doi:10.20944/preprints202406.0338.v1

CNN-CS-NG was evaluated on the percentage of metabolically active cells after a 24 h incubation period. The choice of concentrations was based on previous studies carried out in our laboratory [47]. It is worth mentioning that in the human lines Caco-2 and ARPE-19, a significant proliferation was determined in CS presence. This situation has not been observed in SHSY5Y cultures. However, the percentage of cell viability obtained was ≥ 85%. There is scarce information of the CS NG's effect obtained by ionic gelation on SH-SY5Y cells, Bhattamisra et al., determined that FITC-CS NG at doses less than 10 μg/mL were not cytotoxic using the MTT method [48]. Also, FITC-carboxymethyl-CS-polyamidoamine dendrimers (200 μg/mL) with spherical morphology were successfully uptake after 24 h without affecting the cell viability of primary cultures of neurons and glial cells [49]. Del Prado-Audelo et al., described that although the NG material was biodegradable and biocompatible, cytotoxicity depends on its parameters, i.e. size, charge, surface chemistry, and shape and the concentration used. The interactions with the biological environment and ultimately determine their potential cytotoxicity. In their report, the authors determined that the NG based on Pluronic® F68 was not cytotoxic in a wide range of concentrations after 24 h of treatment in SH-SY5Y cells. In this sense, authors attribute this safety effect to factors that keep resemblance to our system; that is, the high biocompatibility of the polymer, the size, the moderate ζ-potential and the spherical shape of the NG. Furthermore, the spherical morphology has been described as less toxic and less reactive compared to other shapes such as fibres or nanotubes [50]

SH-SY5Y cells cultured with CNN-CS-NG showed rapid internalization. For a constant fluorescence intensity, cellular uptake was time dependent. Lysosomal escape is critical, as this phenomenon limits the efficient administration of drugs in the cytoplasm and was well described for polyethyleneimine (PEI), which is widely used as a vehicle to transfect cDNAs. Since the PEI molecule has numerous protonable amino groups, like CS, it exerts a pH buffer effect (proton sponge effect) that facilitates the escape of late endosomes or lysosomes, whose physiological pH is pH 5.5. When the accumulation of positive charges inside the vesicles is counteracted by a passive entry of chlorine ions to maintain neutrality, this large increase in ion concentration is accompanied by the entry of water molecules that cause vesicle swelling and the rupture of its membrane, and consequently the release of PEI NG and plasmids into the cytoplasm [24,34]. Similarly, in our previous report it has been proven that cationic polymeric NG have pH buffering capacity and facilitate the lysosomal escape in ARPE-19 cells [12]. Here, Fluorescence microscopy has the advantage of providing additional information on the intracellular fluorescence profile. A punctate fluorescence pattern is often considered an indication of the tracer. The compound is trapped in endosomes, while a diffuse label in the cytoplasm implies leakage of endosomal vesicles. However, it should be noted that this tracer cannot distinguish between endosomal escape by formation of pores in the lysosomal membrane or bursting. However, it can give an indication that the additional findings concerning intracellular trafficking events that denoted the preferential nuclear localization and the escape of CNN NG from degradative lysosomal pathways [48,50].

In previous reports, animals were used to detect nanosystems in the brain. The presence of red or green fluorescence was analysed depending on the probe used. DAPI was used to label the cell nuclei in certain works, such as this in report. In reference to this assay, it is important to highlight that the taken images showed red fluorescent areas not only in the tissue of the mice that received CNN-CS-NG, but also in the control animals. As Khalin et al., also indicated, the control tissue has autofluorescence, that is, fluorescence not generated by the NG, but by the brain structures themselves, e.g. lipofuscin accumulation [15]. In any case, after correcting the levels of the positive signal above the autofluorescence signal, it is evident that the CNN-CS-NG were able to reach the brain since the fluorescence intensity increased between 2 and 3 times. In a similar way, CS-TPP based NG functionalized with PEG and loaded with fluorescein isothiocyanate (FITC) were administered i.p. in mice to define their ability to cross the BBB and to reach the CNS [51]. Among the analyse areas (hippocampus, cortex, striatum, corpus callosum and thalamus), a predominant accumulation of NG in the hippocampus stands out in this report. Also, in accordance with our findings, FITC CS NG functionalized with PEG were detected closely in contact with nuclear structures as showed by DAPI staining and inside neuronal cytoplasm, thus indicating in this way their capability in being

 doi:10.20944/preprints202406.0338.v1

endocited by cells. On the other hand, green fluorescent protein-CS nanosystems generated by complex coacervation method, could efficiently cross the BBB. However, authors did not specify which brain area was analysed; beyond this detail, their results suggested that GFP-CS nanosystems could be efficient delivery vehicle for targeted therapies against brain cancers, between other brain diseases [10]. Fluorescent polystyrene NP with carboxylated- or polyethylene glycol-modified (PEGylated) surfaces were delivered into adult female mice. The exact anatomical distribution of the particles was examined by confocal microscopy after a short and a long-time distribution period. Authors found NP signal with different fluorescent intensities in brain, placenta, kidney, spleen, and liver after a single administration and displayed distinct clearing after 4 days. Interesting, both type of NP was detected in those detoxify organs. However, those organs protected by complex physiological barriers (brain and placenta), only experimented the presence of carboxylated NP. A possible explanation lies in the fact that PEGylation reduced the attachment of particles to vessel walls [52].

Kaur et al. analysed brain tissues excised from rats that received quantum-dots PLGA-CS administered via the nasal route. Those particles were able to internalize into brain after 30 min of administration and an increasing red fluorescent intensity could be observed after 2 and 4 h of internalization in the left and right lobe as well as in the cerebellum [53]. Albumin/PLGA nanosystems functionalized with photoactive compound aluminium chloride phthalocyanine were detected as agglomerates (fluorescent dots) at the striatum or hippocampal regions [27]. Also, brain sections exhibited rhodamine fluorescence corresponded to the presence of solid lipid NP in the cerebral parenchyma. Particularly, red vesicles were detected inside the nervous cells and in the vasculature [43]. A series of derivatives of lipidized neurotransmitters, called NT-lipidoids, were doped into lipid NP incapable of crossing the BBB. This doping allowed the impermeability of the latter to be overcome, which was evidenced by the strong presence of tdTomato (fluorescent probe) signal in multiple regions of the brain, including cerebral cortex, hippocampus, and cerebellum. In that report, the red fluorescence signal from hippocampal cells was weaker than that in cerebral cortex and cerebellum, indicating delivery efficiency up to this small region of the brain [54]. Khalin et al., [15] found that red fluorescent signal present in the brain was 2-fold higher for rhodamine-PLGA NP compared with PBS (vehicle). Finally, in a recent report, the presence of biodegradable poly(L-lactide) or non-biodegradable poly(perfluorodecyl acrylate) based-NP in the brain of uninjured and brain-traumatized rats was evaluated. The fluorescent dye N-(2,6-diisopropylphenyl)-perylene-3,4-dicarboximide was used as a marker for the fluorescence measurements. Greater NP absorption was observed at 4 and 24 h after injection in the spleen and liver, followed by the kidney and brain, with minimal concentrations in the heart and lungs. Particularly, greater fluorescent labelling was observed in the traumatized hemisphere, especially in the perilesional area, although there was signal (to a lesser extent) in areas far from the injury site and the contralateral hemisphere. Thus, the assayed NP could be well-thought-out as potentially effective vehicles or markers of newly advanced drugs with low or even no BBB permeation [55].

5. Conclusions

The cutting edge in nanotechnology generates optimism to overcome the growing challenges in biomedical sciences through effective engineering of NG. Particularly, the present assayed CNN-CS-NG were able to reach the brain, demonstrating the ability to cross the BBB. Therefore, the obtained findings in this research can be useful in the field of neuro-nanomedicine when designing drug vehicles with the purpose of delivering drugs to the CNS.

Supplementary Materials: The following supporting information can be downloaded at the website of this paper posted on Preprints.org. Figure S1: ^{1}H NMR spectra of CS; Figure S2: Microscopic brain images of 250 μg/ml CNN-CS-NG-treated mice (magnification of 10X, Scale bar 100 μm). Video S1: Cytoplasmatic and nuclear localization of CNN-CS-NG (red) in SH-SY5Y cells after 24 h of incubation. Images from all z-stacks are visualized through the rotation on the Y axis (FIJI software). Nuclei were stained with DAPI (blue).

Author Contributions: E.RL. (methodology and investigation); C.SL. (methodology, investigation, and formal analysis); B.B. (methodology and investigation); C.C.S. (methodology, investigation, and resources); A.A.

 doi:10.20944/preprints202406.0338.v1

(conceptualization, methodology, investigation, resources, formal analysis, writing-review, and editing); O.E.P. (conceptualization, methodology, validation, resources, writing-review and editing, supervision, project mentor). All authors have read and agreed to the published version of the manuscript.

Funding: Universidad de Buenos Aires, Agencia Nacional de Promoción de Ciencia y Tecnológica and Consejo Nacional de Investigaciones Científicas y Técnicas.

Institutional Review Board Statement: The animal study protocol was approved by the Institutional Ethics Committee (CICUAL, Protocol No. 0024 - University of Buenos Aires).

Informed Consent Statement: Not applicable.

Institutional Review Board Statement: Not applicable.

Data Availability Statement: The data presented in this study are available on request from the corresponding author. The data are not publicly available due to privacy.

Conflicts of Interest: The authors declare no conflicts of interest.

Abbreviations

A.U.: arbitrary units; BBB: blood brain barrier; CLSM: confocal laser scanning microscopy; CNN: tricarbocyanine; CNN-CS-NG: tricarbocyanine-chitosan based nanogels; CNS: central nervous system; CS: chitosan; CS-NG: chitosan based nanogels; DD: degree of deacetylation; DLS: dynamic light scattering; FTIR: Fourier transform Infrared Spectroscopy; HIUS: high intensity ultrasound; i.p.: intraperitoneal; IFP: intracellular fluorescence profile; NG: nanogels; NP: nanoparticles; MeOH: methanol; MTT: 3-(4, 5-dimethylthiazol-2-yl)-2, 5-diphenyltetrazolium bromide; PdI: polydispersity index; SH-SY5Y: neuroblastoma cell line; TEM: transmission electron microscopy; TPP: sodium tripolyphosphate.

References

1. Feigin, V.L.; Krishnamurthi, R. V.; Theadom, A.M.; et al.; Zaki, M.E. Global, Regional, and National Burden of Neurological Disorders during 1990–2015: A Systematic Analysis for the Global Burden of Disease Study 2015. *Lancet Neurol* **2017**, *16*, 877–897, doi:10.1016/S1474-4422(17)30299-5.
2. Owolabi, M.; Leonardi, M.; Bassetti, C.; et al.; Servadei, F. Global Synergistic Actions to Improve Brain Health for Human Development. *Nat Rev Neurol* **2023**, *19*, 371–383, doi:10.1038/s41582-023-00808-z.
3. Liu, D.; Yang, F.; Xiong, F.; Gu, N. The Smart Drug Delivery System and Its Clinical Potential. *Theranostics* 2016, *6*, 1306–1323.
4. Pardridge, W.M. A Historical Review of Brain Drug Delivery. *Pharmaceutics* **2022**, *14*, doi:10.3390/pharmaceutics14061283.
5. Li, J.; Zheng, M.; Shimoni, O.; Banks, W.A.; Bush, A.I.; Gamble, J.R.; Shi, B. Development of Novel Therapeutics Targeting the Blood–Brain Barrier: From Barrier to Carrier. *Advanced Science* **2021**, *8*, 2101090, doi:10.1002/ADVS.202101090.
6. Sun, D.; Gao, W.; Hu, H.; Zhou, S. Why 90% of Clinical Drug Development Fails and How to Improve It? *Acta Pharm Sin B* 2022, *12*, 3049–3062.
7. Agrahari, V.; Kumar, P. Novel Approaches for Overcoming Biological Barriers. *Pharmaceutics* **2022**, *14*, 4–7, doi:10.3390/pharmaceutics14091851.
8. Tan, Q.; Zhao, S.; Xu, T.; Wang, Q.; Lan, M.; Yan, L.; Chen, X. Getting Drugs to the Brain: Advances and Prospects of Organic Nanoparticle Delivery Systems for Assisting Drugs to Cross the Blood-Brain Barrier. *J Mater Chem B* **2022**, *10*, 9314–9333, doi:10.1039/d2tb01440h.
9. Sarkar, A.; Fatima, I.; Mohammad Sajid Jamal, Q.; Sayeed, U.; Kalim A. Khan, M.; Akhtar, S.; Amjad Kamal, M.; Farooqui, A.; Haris Siddiqui, M. Nanoparticles as a Carrier System for Drug Delivery Across Blood Brain Barrier. *Curr Drug Metab* **2017**, *18*, 129–137, doi:10.2174/1389200218666170113125132.

10. Khan, I.N.; Navaid, S.; Waqar, W.; Hussein, D.; Ullah, N.; Khan, M.U.A.; Hussain, Z.; Javed, A. Chitosan-Based Polymeric Nanoparticles as an Efficient Gene Delivery System to Cross Blood Brain Barrier: In Vitro and In Vivo Evaluations. *Pharmaceuticals* **2024**, *17*, 169, doi:10.3390/ph17020169.
11. Crini, G. Historical Review on Chitin and Chitosan Biopolymers. *Environ Chem Lett* 2019, *17*, 1623–1643.
12. Buosi, F.S.*; Alaimo, A.*; Di Santo, M.C.; Elías, F.; García Liñares, G.; Acebedo, S.L.; Castañeda Cataña, M.A.; Spagnuolo, C.C.; Lizarraga, L.; Martínez, K.D.; et al. Resveratrol Encapsulation in High Molecular Weight Chitosan-Based Nanogels for Applications in Ocular Treatments: Impact on Human ARPE-19 Culture Cells. *Int J Biol Macromol* **2020**, *165*, 804–821, doi:10.1016/j.ijbiomac.2020.09.234.
13. Silva Nieto, R.; Samaniego López, C.; Moretton, M.A.; Lizarraga, L.; Chiappetta, D.A.; Alaimo, A.; Pérez, O.E. Chitosan-Based Nanogels Designed for Betanin-Rich Beetroot Extract Transport: Physicochemical and Biological Aspects. *Polymers (Basel)* **2023**, *15*, doi:10.3390/polym15193875.
14. Algharib, S.A.; Dawood, A.; Zhou, K.; Chen, D.; Li, C.; Meng, K.; Zhang, A.; Luo, W.; Ahmed, S.; Huang, L.; et al. Preparation of Chitosan Nanoparticles by Ionotropic Gelation Technique: Effects of Formulation Parameters and in Vitro Characterization. *J Mol Struct* **2022**, *1252*, 132129, doi:10.1016/J.MOLSTRUC.2021.132129.
15. Khalin, I.; Severi, C.; Heimburger, D.; Wehn, A.; Hellal, F.; Reisch, A.; Klymchenko, A.S.; Plesnila, N. Dynamic Tracing Using Ultra-Bright Labeling and Multi-Photon Microscopy Identifies Endothelial Uptake of Poloxamer 188 Coated Poly(Lactic-Co-Glycolic Acid) Nano-Carriers in Vivo. *Nanomedicine* **2022**, *40*, 102511, doi:10.1101/2020.11.19.385062.
16. Vargas-Nadal, G.; Köber, M.; Nsamela, A.; Terenziani, F.; Sissa, C.; Pescina, S.; Sonvico, F.; Gazzali, A.M.; Wahab, H.A.; Grisanti, L.; et al. Fluorescent Multifunctional Organic Nanoparticles for Drug Delivery and Bioimaging: A Tutorial Review. *Pharmaceutics* **2022**, *14*, 2498, doi:10.3390/pharmaceutics14112498.
17. Samaniego Lopez, C.; Amparo, M.; Huvelle, L.; Uhrig, M.L.; Coluccio, F.; Spagnuolo, C.C. *Electronic Supplementary Information (ESI) Recognition of Saccharides in the NIR Region with a Novel Fluorogenic Boronolectin: In Vitro and Live Cells Labeling*; 2015;
18. Bihari, P.; Vippola, M.; Schultes, S.; Praetner, M.; Khandoga, A.G.; Reichel, C.A.; Coester, C.; Tuomi, T.; Rehberg, M.; Krombach, F. Optimized Dispersion of Nanoparticles for Biological in Vitro and in Vivo Studies. *Part Fibre Toxicol* **2008**, *5*, 1–14, doi:10.1186/1743-8977-5-14.
19. Buosi, S.F.; Alaimo, A.; Di Santo, M.C.; Elías, F.; García, G.; Acebedo, S.L.; Alejandra, M.L.; Mayra Alejandra, Castañeda Spagnuolo, C.C.; Lizarraga, L.; Martínez, K.D.; et al. Resveratrol Encapsulation in High Molecular Weight Chitosan-Based Nanogels for Applications in Ocular Treatments : Impact on Human ARPE-19 Culture Cells. *Int J Biol Macromol* **2020**, *165*, 804–821, doi:10.1016/j.ijbiomac.2020.09.234.
20. Prudkin Silva, C.; Richmond, L.; Martínez, K.D.; Martínez, J.H.; Martínez, K.D.; Farías, M.E.; Pérez, O.E.O.E.; Leskow, F.C.; Pérez, O.E.O.E. Proposed Molecular Model for Electrostatic Interactions between Insulin and Chitosan. Nano-Complexation and Activity in Cultured Cells. *Colloids Surf A Physicochem Eng Asp* **2018**, *537*, 425–434, doi:10.1016/j.colsurfa.2017.10.040.
21. Martin, E.R.; Gandawijaya, J.; Oguro-Ando, A. A Novel Method for Generating Glutamatergic SH-SY5Y Neuron-like Cells Utilizing B-27 Supplement. *Front Pharmacol* **2022**, *13*, doi:10.3389/fphar.2022.943627.
22. Martinez, J.H.; Alaimo, A.; Gorojod, R.M.; Porte Alcon, S.; Fuentes, F.; Coluccio Leskow, F.; Kotler, M.L. Drp-1 Dependent Mitochondrial Fragmentation and Protective Autophagy in Dopaminergic SH-SY5Y Cells Overexpressing Alpha-Synuclein. *Molecular and Cellular Neuroscience* **2018**, *88*, 107–117, doi:10.1016/j.mcn.2018.01.004.

23. Boeneman, K.; Delehanty, J.B.; Blanco-Canosa, J.B.; Susumu, K.; Stewart, M.H.; Oh, E.; Huston, A.L.; Dawson, G.; Ingale, S.; Walters, R.; et al. Selecting Improved Peptidyl Motifs for Cytosolic Delivery of Disparate Protein and Nanoparticle Materials. *ACS Nano* **2013**, *7*, 3778–3796, doi:10.1021/nn400702r.
24. Martens, T.F.; Remaut, K.; Demeester, J.; De Smedt, S.C.; Braeckmans, K. Intracellular Delivery of Nanomaterials: How to Catch Endosomal Escape in the Act. *Nano Today* **2014**, *9*, 344–364, doi:10.1016/j.nantod.2014.04.011.
25. Atabakhshi-Kashi, M.; Carril, M.; Mahdavi, H.; Parak, W.J.; Carrillo-Carrion, C.; Khajeh, K. In Vitro Cellular Uptake Studies of Self-Assembled Fluorinated Nanoparticles Labelled with Antibodies. *Nanomaterials* **2021**, *11*, doi:10.3390/nano11081906.
26. Berardino, B.G.; Ballarini, F.; Chertoff, M.; Igaz, L.M.; Cánepa, E.T. Nutritional Stress Timing Differentially Programs Cognitive Abilities in Young Adult Male Mice. *Nutr Neurosci* **2022**, *25*, 286–298, doi:10.1080/1028415X.2020.1751507.
27. Monge-Fuentes, V.; Biolchi Mayer, A.; Lima, M.R.; Geraldes, L.R.; Zanotto, L.N.; Moreira, K.G.; Martins, O.P.; Piva, H.L.; Felipe, M.S.S.; Amaral, A.C.; et al. Dopamine-Loaded Nanoparticle Systems Circumvent the Blood–Brain Barrier Restoring Motor Function in Mouse Model for Parkinson's Disease. *Sci Rep* **2021**, *11*, doi:10.1038/s41598-021-94175-8.
28. Paxinos, G.; Franklin, K.B.J. Paxinos and Franklin's The Mouse Brain in Stereotaxic Coordinates. **1998**, *4th Ed.*
29. Allen Institute for Brain Science Atlas Brain Map.
30. Jiang, Y.; Fu, C.; Wu, S.; Liu, G.; Guo, J.; Su, Z. Determination of the Deacetylation Degree of Chitooligosaccharides. *Mar Drugs* **2017**, *15*, doi:10.3390/md15110332.
31. Picone, C.S.F.; Cunha, R.L. Chitosan-Gellan Electrostatic Complexes: Influence of Preparation Conditions and Surfactant Presence. *Carbohydr Polym* **2013**, *94*, 695–703, doi:10.1016/j.carbpol.2013.01.092.
32. Khattab, T.A.; Kassem, N.F.; Adel, A.M.; Kamel, S. Optical Recognition of Ammonia and Amine Vapor Using "Turn-on" Fluorescent Chitosan Nanoparticles Imprinted on Cellulose Strips. *J Fluoresc* **2019**, *29*, 693–702, doi:10.1007/s10895-019-02381-5.
33. Vimal, S.; Abdul Majeed, S.; Taju, G.; Nambi, K.S.N.; Sundar Raj, N.; Madan, N.; Farook, M.A.; Rajkumar, T.; Gopinath, D.; Sahul Hameed, A.S. Chitosan Tripolyphosphate (CS/TPP) Nanoparticles: Preparation, Characterization and Application for Gene Delivery in Shrimp. *Acta Trop* **2013**, *128*, 486–493, doi:10.1016/j.actatropica.2013.07.013.
34. Smith, S.A.; Selby, L.I.; Johnston, A.P.R.; Such, G.K. The Endosomal Escape of Nanoparticles: Toward More Efficient Cellular Delivery. *Bioconjug Chem* **2019**, *30*, 263–272, doi:10.1021/acs.bioconjchem.8b00732.
35. Cupic, K.I.; Rennick, J.J.; Johnston, A.P.R.; Such, G.K. Controlling Endosomal Escape Using Nanoparticle Composition: Current Progress and Future Perspectives. *Nanomedicine (Lond)* **2019**, *14*, 215–223, doi:10.2217/NNM-2018-0326.
36. Vermeulen, L.M.P.; Fraire, J.C.; Raes, L.; De Meester, E.; De Keulenaer, S.; Van Nieuwerburgh, F.; De Smedt, S.; Remaut, K.; Braeckmans, K. Photothermally Triggered Endosomal Escape and Its Influence on Transfection Efficiency of Gold-Functionalized JetPEI/PDNA Nanoparticles. *Int J Mol Sci* **2018**, *19*, doi:10.3390/ijms19082400.
37. Zhu, J.Y.; Lei, Q.; Yang, B.; Jia, H.Z.; Qiu, W.X.; Wang, X.; Zeng, X.; Zhuo, R.X.; Feng, J.; Zhang, X.Z. Efficient Nuclear Drug Translocation and Improved Drug Efficacy Mediated by Acidity-Responsive Boronate-Linked Dextran/Cholesterol Nanoassembly. *Biomaterials* **2015**, *52*, 281–290, doi:10.1016/j.biomaterials.2015.02.048.

 doi:10.20944/preprints202406.0338.v1

38. Carton, F.; Malatesta, M. *Assessing the Interactions between Nanoparticles and Biological Barriers in Vitro: A New Challenge for Microscopy Techniques in Nanomedicine*; 2022; Vol. 66;.
39. Álamo, P.; Pallarès, V.; Céspedes, M.V.; Falgàs, A.; Sanchez, J.M.; Serna, N.; Sánchez-garcía, L.; Voltà-duràn, E.; Morris, G.A.; Sánchez-chardi, A.; et al. Fluorescent Dye Labeling Changes the Biodistribution of Tumor-targeted Nanoparticles. *Pharmaceutics* **2020**, *12*, 1–18, doi:10.3390/pharmaceutics12111004.
40. Marcelo, G.A.; Galhano, J.; Oliveira, E. Applications of Cyanine-Nanoparticle Systems in Science: Health and Environmental Perspectives. *Dyes and Pigments* **2022**, *208*, doi:10.1016/j.dyepig.2022.110756.
41. Lombardo, S.M.; Schneider, M.; Türeli, A.E.; Türeli, N.G. Key for Crossing the BBB with Nanoparticles: The Rational Design. *Beilstein Journal of Nanotechnology* 2020, *11*, 866–883.
42. Jiang, L.Q.; Wang, T.Y.; Webster, T.J.; Duan, H.J.; Qiu, J.Y.; Zhao, Z.M.; Yin, X.X.; Zheng, C.L. Intracellular Disposition of Chitosan Nanoparticles in Macrophages: Intracellular Uptake, Exocytosis, and Intercellular Transport. *Int J Nanomedicine* **2017**, *12*, 6383–6398, doi:10.2147/IJN.S142060.
43. Ortega, E.; Blanco, S.; Ruiz, A.; Peinado, M.Á.; Peralta, S.; Morales, M.E. Lipid Nanoparticles for the Transport of Drugs like Dopamine through the Blood-Brain Barrier. *Journal of Nanoparticle Research* **2021**, *23*, doi:10.1007/s11051-021-05218-0.
44. ŞEKO, I.; SAHÍN, A.; TONBUL, H.; ÇAPAN, Y. Brain-Targeted Nanoparticles to Overcome the Blood-Brain Barrier. *Journal of Pharmaceutical Technolgy* **2020**, *1*, 26–40, doi:10.37662/jpt.2020.4.
45. Nance, E.A.; Woodworth, G.F.; Sailor, K.A.; Shih, T.Y.; Xu, Q.; Swaminathan, G.; Xiang, D.; Eberhart, C.; Hanes, J. A Dense Poly(Ethylene Glycol) Coating Improves Penetration of Large Polymeric Nanoparticles within Brain Tissue. *Sci Transl Med* **2012**, *4*, doi:10.1126/scitranslmed.3003594.
46. Papadia, K.; Markoutsa, E.; Antimisiaris, S.G. How Do the Physicochemical Properties of Nanoliposomes Affect Their Interactions with the HCMEC/D3 Cellular Model of the BBB? *Int J Pharm* **2016**, *509*, 431–438, doi:10.1016/j.ijpharm.2016.06.019.
47. Di Santo, M.C.; Alaimo, A.; Dominguez Rubio, A.; De Matteo, R.; Pérez, O.E. Biocompatibility Analysis of High Molecular Weight Chitosan Obtained from Pleoticus Muelleri Shrimps . Evaluation in Prokaryotic and Eukaryotic Cells . *Biochem Biophys Rep* **2020**, *24*, 100842, doi:10.1016/j.bbrep.2020.100842.
48. Bhattamisra, S.K.; Shak, A.T.; Xi, L.W.; Safian, N.H.; Choudhury, H.; Lim, W.M.; Shahzad, N.; Alhakamy, N.A.; Anwer, M.K.; Radhakrishnan, A.K.; et al. Nose to Brain Delivery of Rotigotine Loaded Chitosan Nanoparticles in Human SH-SY5Y Neuroblastoma Cells and Animal Model of Parkinson's Disease. *Int J Pharm* **2020**, *579*, doi:10.1016/j.ijpharm.2020.119148.
49. Salgado, A.J.; Oliveira, J.M.; Pirraco, R.P.; Pereira, V.H.; Fraga, J.S.; Marques, A.P.; Neves, N.M.; Mano, J.F.; Reis, R.L.; Sousa, N. Carboxymethylchitosan/Poly(Amidoamine) Dendrimer Nanoparticles in Central Nervous Systems-Regenerative Medicine: Effects on Neuron/Glial Cell Viability and Internalization Efficiency. *Macromol Biosci* **2010**, *10*, 1130–1140, doi:10.1002/mabi.201000005.
50. Del Prado-Audelo, M.L.; Magaña, J.J.; Mejía-Contreras, B.A.; Borbolla-Jiménez, F. V.; Giraldo-Gomez, D.M.; Piña-Barba, M.C.; Quintanar-Guerrero, D.; Leyva-Gómez, G. In Vitro Cell Uptake Evaluation of Curcumin-Loaded PCL/F68 Nanoparticles for Potential Application in Neuronal Diseases. *J Drug Deliv Sci Technol* **2019**, *52*, 905–914, doi:10.1016/j.jddst.2019.05.042.
51. Monsalve, Y.; Tosi, G.; Ruozi, B.; Belletti, D.; Vilella, A.; Zoli, M.; Vandelli, M.A.; Forni, F.; López, B.L.; Sierra, L. PEG-g-Chitosan Nanoparticles Functionalized with the Monoclonal Antibody OX26 for Brain Drug Targeting. *Nanomedicine* **2015**, *10*, 1735–1750, doi:10.2217/nnm.15.29.

 doi:10.20944/preprints202406.0338.v1

52. Kenesei, K.; Murali, K.; Czéh, Á.; Piella, J.; Puntes, V.; Madarász, E. Enhanced Detection with Spectral Imaging Fluorescence Microscopy Reveals Tissue- and Cell-Type-Specific Compartmentalization of Surface-Modified Polystyrene Nanoparticles. *J Nanobiotechnology* **2016**, *14*, doi:10.1186/s12951-016-0210-0.
53. Kaur, S.; Manhas, P.; Swami, A.; Bhandari, R.; Sharma, K.K.; Jain, R.; Kumar, R.; Pandey, S.K.; Kuhad, A.; Sharma, R.K.; et al. Bioengineered PLGA-Chitosan Nanoparticles for Brain Targeted Intranasal Delivery of Antiepileptic TRH Analogues. *Chemical Engineering Journal* **2018**, *346*, 630–639, doi:10.1016/j.cej.2018.03.176.
54. Ma, F.; Yang, L.; Sun, Z.; Chen, J.; Rui, X.; Glass, Z.; Xu, Q. Neurotransmitter-Derived Lipidoids (NT-Lipidoids) for Enhanced Brain Delivery through Intravenous Injection. *Sci Adv* . **2020**, *6*, eabb4429, doi:10.1126/sciadv.abb4429.
55. Sharma, H.S.; Kreuter, J.; Latronico, T.; of Bari Aldo Moro, U.; Himakarnika Alluri, I.; Serrano Sponton, L.; Sponton, S.L. In-Vivo Time Course of Organ Uptake and Blood-Brain-Barrier Permeation of Poly(L-Lactide) and Poly(Perfluorodecyl Acrylate) Nanoparticles with Different Surface Properties in Unharmed and Brain-Traumatized Rats. *Front Neurol* . 2023, *6*, 994877.